Inorganic Chemistry
Cite This: Inorg. Chem. 2018, 57, 3529−3539
Forum Article
pubs.acs.org/IC

Design of Zn-, Cu-, and Fe-Coordination Complexes Confined in a Self-Assembled Nanocage

Cédric Colomban,[†] Vlad Martin-Diaconescu,[‡] Teodor Parella,[§] Sébastien Goeb,[∥] Cristina García-Simón,[†] Julio Lloret-Fillol,[‡] Miquel Costas,*[,†] and Xavi Ribas*[,†]

[†]Institut de Química Computacional i Catàlisi, Universitat de Girona, Campus Montilivi, 17003 Girona, Catalonia, Spain
[‡]Institute of Chemical Research of Catalonia (ICIQ), The Barcelona Institute of Science and Technology, Avinguda Paisos Catalans 16, 43007 Tarragona, Catalonia, Spain
[§]Servei de RMN, Facultat de Ciències, Universitat Autònoma de Barcelona, Campus UAB, E-08193 Bellaterra, Catalonia, Spain
[∥]Université d'Angers, CNRS UMR 6200, Laboratoire MOLTECH-Anjou, 2 bd Lavoisier, 49045 Angers Cedex, France

Supporting Information

ABSTRACT: The encapsulation of coordination complexes in a tetragonal prismatic nanocage ($\mathbf{1}\cdot(\mathbf{BAr^F})_8$) built from Zn-porphyrin and macrocyclic Pd-clip-based synthons is described. The functional duality of the guest ligand $\mathbf{L_1}$ allows for its encapsulation inside the cage $\mathbf{1}\cdot(\mathbf{BAr^F})_8$, along with the simultaneous coordination of Zn^{II}, Cu^{II}, or Fe^{III} metal ions. Remarkably, the coordination chemistry inside the host−guest adduct $\mathbf{L_1}\subset\mathbf{1}\cdot(\mathbf{BAr^F})_8$ occurs in both solution solution and solid state. The resulting confined metallocomplexes have been characterized by means of UV-vis, ESI-HRMS, NMR, and EPR techniques. Furthermore, the emission of the Zn-porphyrin fluorophores of $\mathbf{1}\cdot(\mathbf{BAr^F})_8$ is strongly quenched by the encapsulation of paramagnetic complexes, representing a remarkable example of guest-dependent tuning of the host fluorescence.

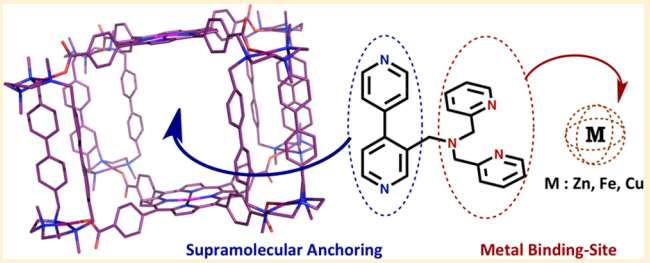

INTRODUCTION

Zn, Cu, and Fe metal ions are bioelements present in trace levels in virtually all living organisms.[1] They are essential for life, and many of their basic functions arise from their participation in the active site of metalloproteins, which perform a wide range of chemical transformations in a highly effective manner that have yet to be achieved by artificial systems. The isolated and constrained environment provided by enzymatic cavities maximizes both their efficiency and selectivity, because of a highly efficient substrate recognition ability, along with control of the nuclearity of the metal center.[2] Therefore, designing or discovering mechanisms and methodologies to generate and stabilize confined metallocomplexes in synthetic systems is key to the exploration of structural and functional models of the unique chemistry found in metalloenzymes. Aiming at improving the classical biomimetic strategy for the conception of a model compound, which relies on the mimicry of the first coordination sphere of the metal site, porous supramolecular entities have been proven to be remarkably efficient as models of the second (and further) coordination sphere found in metalloenzymes. Confined metallocomplexes can be obtained following different strategies:

(a) the inclusion of the metallocomplex within a protein scaffold to obtain artificial metalloproteins;[3]
(b) by building an organic architecture over the complex to obtain covalent capsules such as deep cavitands,[4] calix[6]-arenes,[5] or hemicryptophanes;[6]
(c) by solid-state coordination chemistry within heterogeneous structures, such as metal-organic frameworks (MOFs);[7] or
(d) by host−guest encapsulation within self-assembled coordination capsules.[8]

It is in this last category that Fujita, Clever, Raymond and Bergman have shown remarkable host systems where organometallic Mn-,[9] Pt-,[10] Ir-,[11] Rh-,[12] Ru-,[13] or Au-based,[14] complexes and fragments are bound inside metal−organic cages. The recent developments of coordination-driven self-assembly have led to the preparation of discrete architectures displaying various three-dimensional geometries with versatile building blocks.[15] Among them, Zn-porphyrin-based supramolecular structures have attracted much attention. The self-assembly of toogle nanoswitch,[16] molecular barrels with porphyrinic walls,[17] coordination prisms with porphyrinic faces,[18] and even multi-porphyrin cages[19] has been successfully described using different bridging metals (Pd, Pt, Zn). Furthermore, the usefulness of porphyrin-based capsules for versatile applications ranging from binding and separation of fullerenes,[20] spin crossover,[21] cooperative binding of anionic and neutral guest species,[22] to isolation of metallo-catalysts aiming at performing catalysis in a confined space,[23,24] have been recently established.

Special Issue: Self-Assembled Cages and Macrocycles
Received: November 13, 2017
Published: January 2, 2018

DOI: 10.1021/acs.inorgchem.7b02852
Inorg. Chem. 2018, 57, 3529−3539

However, to the best of our knowledge, the confinement of biologically relevant metal ions having a bioinspired first coordination sphere, inside a well-defined self-assembled supramolecular cage, thus modeling a second coordination sphere, has yet to be described.

In this article, we present the design, preparation, and characterization of a novel supramolecular system integrating the principles of self-assembly, host–guest chemistry, and coordination chemistry in both solution and solid-state. We report the study of zinc, copper, and iron-based complexes entrapped in the self-assembled tetragonal prismatic cage $\mathbf{1}\cdot(\mathbf{BAr^F})_8$. The previously reported nanocage $\mathbf{1}\cdot(\mathbf{BAr^F})_8$ consists of two opposing Zn-porphyrins bound by four bridging macrocyclic walls interconnected by Pd^{II}–carboxylate bonds (Figure 1).

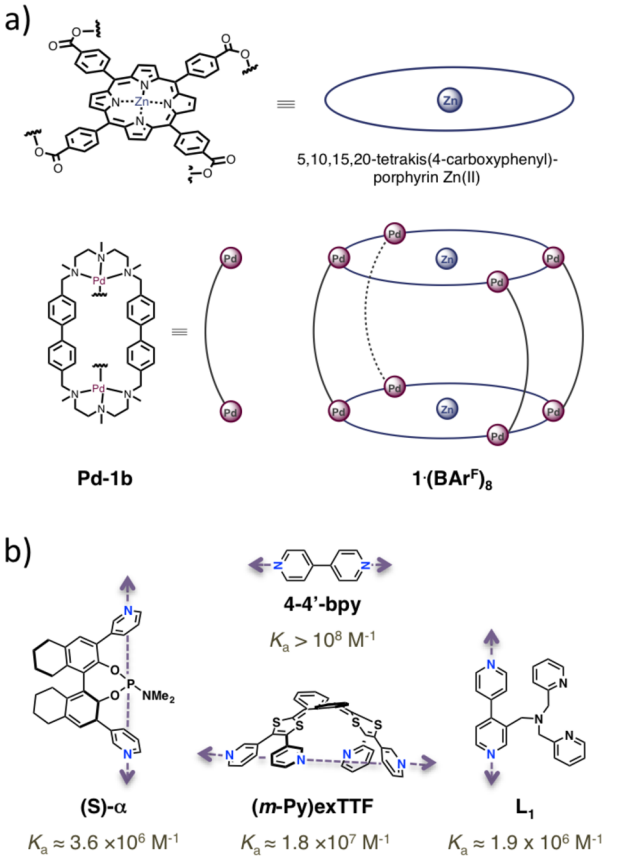

Figure 1. (a) Schematic representation of the building block used for the synthesis of the nanocapsule $\mathbf{1}\cdot(\mathbf{BAr^F})_8$. (b) Binding constants (K_a) to the nanocage $\mathbf{1}\cdot(\mathbf{BAr^F})_8$ for the previously reported pyridine-based ligands ((*S*)-**α**, **4,4′-bpy**),[24] (*m*-Py)exTTF,[25] and the ligand $\mathbf{L_1}$ used in this study. Purple arrows show the directional binding of the guests to both Zn-porphyrin units of $\mathbf{1}\cdot(\mathbf{BAr^F})_8$.

The coordination of exogenous metals within $\mathbf{1}\cdot(\mathbf{BAr^F})_8$ was reached through the encapsulation of the guest $\mathbf{L_1}$, which can (i) strongly bind to the cage via a bipyridine anchor and (ii) coordinate metal ions with its pendent bispicolylamine arm (Figure 1).

We demonstrate that the ligand $\mathbf{L_1}$ and its corresponding Zn^{II}, Cu^{II}, and Fe^{III} complexes are anchored to the vessel $\mathbf{1}\cdot(\mathbf{BAr^F})_8$ through the predictably directional (Zn-porphyrin)···(4,4′-bipyridine)···(Zn-porphyrin) coordination bonds. We observed that the guests $\mathbf{L_1}$ and its corresponding Zn-complex are both freely rotating inside $\mathbf{1}\cdot(\mathbf{BAr^F})_8$ around the Zn···Zn axis. Finally, a guest-dependent tuning of the fluorescence emission of the porphyrin-based capsule $\mathbf{1}\cdot(\mathbf{BAr^F})_8$ upon accommodation of $\mathbf{L_1}$ or the paramagnetic $\mathbf{L_1}$-Cu^{II}- and $\mathbf{L_1}$-Fe^{III}-complexes is described. Overall, this work aims at providing a new tool for exploring coordination chemistry in a confined space, offering a bridge between the supramolecular chemistry of metal–organic cages and the synthetic small-molecule bioinorganic models.

RESULTS AND DISCUSSION

Design and Synthesis of the Ligand $\mathbf{L_1}$. The cage $\mathbf{1}\cdot(\mathbf{BAr^F})_8$ has been reported as an effective receptor for pyridine-based guests, which are strongly bound through the well-known ability of Zn-porphyrins to interact with pyridine moieties (Figure 1b).[24,25] Polypyridyl guests with different intramolecular $N_{pyridine}\cdots N_{pyridine}$ distances can be encapsulated thanks to the structural flexibility of the Pd-carboxylate bonds (Zn···Zn distance in $\mathbf{1}\cdot(\mathbf{BAr^F})_8$ can vary from ∼11 Å to 14 Å). Among them, the guest with the highest binding constant was 4,4′-bipyridine (**4,4′-bpy**) ($K_a > 10^8\ M^{-1}$) attesting for an optimal shape, relative disposition of the pyridines and $N_{pyridine}\cdots N_{pyridine}$ distance.

On the other hand, N_3 ligands based on the bis(2-pyridylmethyl)amine (**BPA**) unit (Figure 2) have been used aiming at

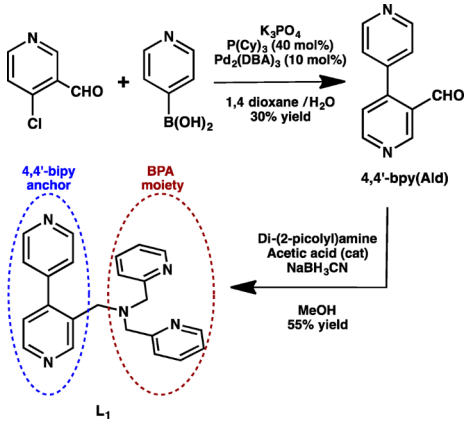

Figure 2. Synthetic strategy toward ligand $\mathbf{L_1}$.

mimicking a poly(histidine) coordination environment commonly found in enzymes. Numerous examples of zinc, copper, and iron complexes of BPA-based ligands have been reported.[26]

Based on (i) the strong affinity between $\mathbf{1}\cdot(\mathbf{BAr^F})_8$ and **4,4′-bpy**, and (ii) the well-described ability of the **BPA** motif to coordinate biologically relevant metals, we designed ligand $\mathbf{L_1}$, which consists of a derivative of **4,4′-bpy(Ald)** with two pendent pyridines connected via a pivotal amine at the *meta*-position. The ligand $\mathbf{L_1}$ was synthesized following a two-step synthetic strategy (Figure 2). First, a carbaldehyde substituent was incorporated at the *meta*-position of the **4,4′-bpy(Ald)** by means of a Suzuki–Miyaura cross-coupling reaction.[27] Then, reductive amination between **4,4′-bpy(Ald)** and bis(2-pyridylmethyl)amine (**BPA**) gave the targeted ligand $\mathbf{L_1}$ in 55% yield.

Synthesis and Characterization of $\mathbf{L_1}$–Metal Complexes. Aiming at avoiding the putative electrostatic repulsion between the metal-cations and the highly charged (8+) nanocapsule, the study focused on the coordination of metal-ion salts with strongly bound halogen counterions (Cl, Br), which forms neutral metal halides. We first investigated the ability of $\mathbf{L_1}$ to form metallo-complexes through metal coordination at its

DOI: 10.1021/acs.inorgchem.7b02852
Inorg. Chem. 2018, 57, 3529–3539

BPA moiety. The air-stable zinc(II), copper(II), and iron(III) complexes of general formula $\mathbf{L_1Zn^{II}(Cl)_2}$, $\mathbf{L_1Cu^{II}(Br)_2}$, and $\mathbf{L_1Fe^{III}(Cl)_3}$ were prepared by reacting $\mathbf{L_1}$ with the appropriate Zn^{II}, Cu^{II}, and Fe^{III} halide salts in MeOH, CH_3CN, and THF, respectively, at room temperature. The metalation occurred immediately and the targeted compounds were precipitated with diethyl ether, isolated by filtration, and characterized by high-resolution mass spectrometry (ESI-HRMS) (see Figures S1, S2, and S3 in the Supporting Information). The diamagnetic $\mathbf{L_1Zn^{II}(Cl)_2}$ complex was also characterized by one-dimensional (1D) and two-dimensional (2D) nuclear magnetic resonance (NMR) (see Figures S4 and S5 in the Supporting Information). The paramagnetic $\mathbf{L_1Cu^{II}(Br)_2}$ and $\mathbf{L_1Fe^{III}(Cl)_3}$ complexes afforded single crystals suitable for X-ray diffraction (XRD) (see Figure 3).

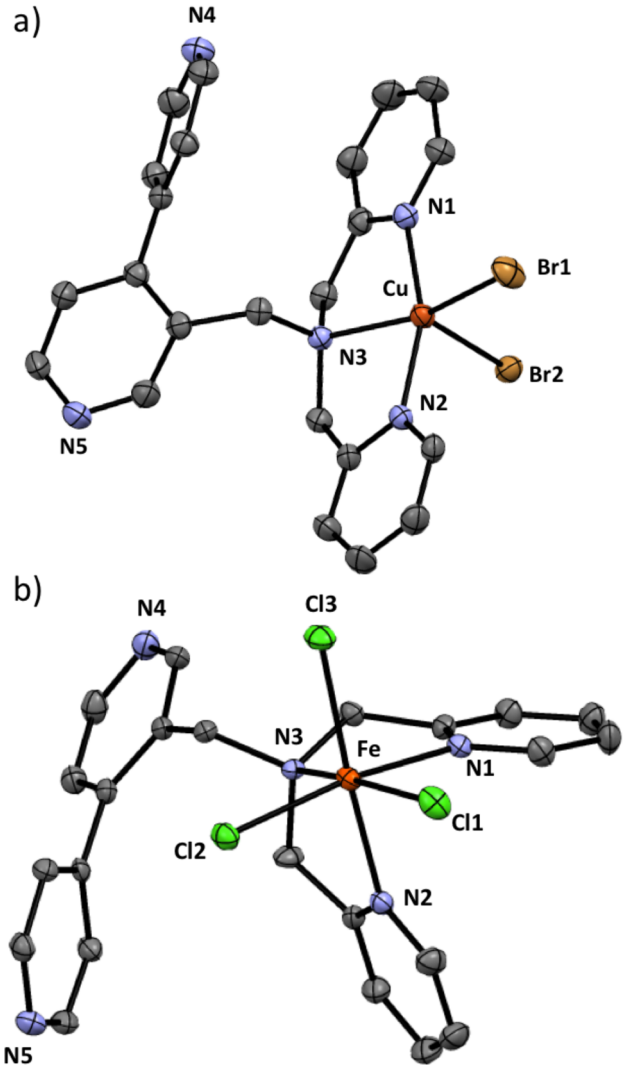

Figure 3. ORTEP (ellipsoids, 50% probability) diagrams of the X-ray crystal structures of (a) $\mathbf{L_1Cu^{II}(Br)_2}$ and (b) $\mathbf{L_1Fe^{III}(Cl)_3}$.

The structure of the monomeric complexes $\mathbf{L_1Cu^{II}(Br)_2}$[28] and $\mathbf{L_1Fe^{III}(Cl)_3}$[29] show Cu and Fe centers in standard square pyramidal and distorted octahedral geometries, respectively (Figure 3). Importantly, the **4,4′-Bpy** motif in these structures do not interact with the metal ions, remaining available for the expected anchoring within $\mathbf{1\cdot(BAr^F)_8}$. Furthermore, the $N_{Py}\cdots N_{Py}$ distance in the **4,4′-bpy** moieties of $\mathbf{L_1Cu^{II}(Br)_2}$ and $\mathbf{L_1Fe^{III}(Cl)_3}$ was found to be, respectively, 7.102 and 7.134 Å, which are perfectly suitable distances to bind simultaneously to both Zn-porphyrin units of $\mathbf{1\cdot(BAr^F)_8}$.

Preparation and Characterization of the Host–Guest Adduct $\mathbf{L_1\subset 1\cdot(BAr^F)_8}$. We then investigated the host–guest interaction between cage $\mathbf{1\cdot(BAr^F)_8}$ and $\mathbf{L_1}$ by UV-vis titration experiments (see Figure S7 in the Supporting Information). Titrations monitored the bathochromic shift of the porphyrin Soret band (from 424 to 427 nm) exhibiting clean isosbestic points, and resulted in a binding constant of $K_a = (1.59 \pm 0.19) \times 10^6\ M^{-1}$. This high association constant is similar to the one previously reported for the pyridine-based ligands **(*S*)-*α*** (Figure 1) and strongly suggests that $\mathbf{L_1}$ is bound inside $\mathbf{1\cdot(BAr^F)_8}$ in a ditopic fashion, similar to that observed for **4,4′-bpy** or **(*S*)-*α***.[24] ESI-HRMS analysis unambiguously supports the formation of $\mathbf{L_1\subset 1\cdot(BAr^F)_8}$ in a 1:1 stoichiometry (Figure S8 in the Supporting Information). Importantly, only traces of the empty $\mathbf{1\cdot(BAr^F)_8}$ could be detected in the MS spectra, reflecting a strong binding also in the gas phase.

The detection of $\mathbf{L_1\subset 1\cdot(BAr^F)_8}$ was further confirmed by tandem MS/MS experiments. Indeed, when the mass-selected $[\mathbf{L_1\subset 1\cdot(BAr^F)_1}]^{7+}$ complex (m/z = 909.9; 7+) was subjected to collision-induced dissociation (CID), an isotopic pattern corresponding to the empty cage $[\mathbf{1\cdot(BAr^F)_1}]^{7+}$ (m/z = 857.3; 7+) was observed; a collision energy of 15 eV was needed to observed a total dissociation (Figure S9 in the Supporting Information).

The ^{1}H NMR spectrum of the $\mathbf{L_1\subset 1\cdot(BAr^F)_8}$ adduct displays well-defined signals between 4.0 and 7.2 ppm (see Figure S10 in the Supporting Information) corresponding to the encapsulated ligand $\mathbf{L_1}$. The assignment of these resonances was performed by the analysis of 2D COSY, NOESY, and HSQC spectra (Figure S11, S12, and S13 in the Supporting Information). When encapsulated, the $\mathbf{L_1}$ signals experience a strong upfield chemical-shift effect, because of the proximity to the porphyrin moieties of the cage. Interestingly, a stronger effect was observed on the aromatic protons belonging to the **4,4′-bpy** moiety of $\mathbf{L_1}$ (resonating between 2.14 ppm and 4.62 ppm). In particular, protons at the α-position of the **4,4′-bpy** unit (resonating at 2.14 and 2.18 ppm) are displaying the strongest upfield shift, confirming their close proximity with the aromatic porphyrin ring resulting from coordination between the **4,4′-bpy** moiety and the Zn porphyrin moieties of $\mathbf{1\cdot(BAr^F)_8}$. On the other hand, the aromatic protons belonging to the **BPA** moiety of $\mathbf{L_1}$ retain the original symmetry of the free ligand and experience a less-intense upfield-chemical shift, with resonances at 5.70, 6.27, 6.56, and 7.27 ppm when encapsulated (7.14, 7.29, 7.61, and 8.47 ppm, respectively, for the free $\mathbf{L_1}$). The latter indicates that the **BPA** moiety of $\mathbf{L_1}$, on average, is farther from the porphyrin rings of $\mathbf{1\cdot(BAr^F)_8}$. Therefore, the two pendent pyridines connected via a pivotal amine present in $\mathbf{L_1}$ interact minimally with the Zn-porphyrins, remaining available for the complexation of exogenous metals.

With respect to the signals belonging to cage $\mathbf{1\cdot(BAr^F)_8}$, the encapsulation of $\mathbf{L_1}$ leads to moderate upfield shifts of the signals corresponding to some of the aromatic protons of the cage (Figure 4). Interestingly, in the ^{1}H NMR spectrum of $\mathbf{L_1\subset 1\cdot(BAr^F)_8}$ at room temperature, the aromatic protons "h" and "j" of the Zn-porphyrins, which are pointing inside the cavity, appeared doubled. At lower temperature (278 K), all signals of the porphyrin units are split into two different signals each, including the pyrrole protons that appear as two separated singlets at 8.64 and 8.61 ppm (see Figure 4, as well as Figure S14 in the Supporting Information). Therefore, the encapsulation of $\mathbf{L_1}$ is breaking the D_{4h} symmetry initially found in the empty

DOI: 10.1021/acs.inorgchem.7b02852
Inorg. Chem. 2018, 57, 3529–3539

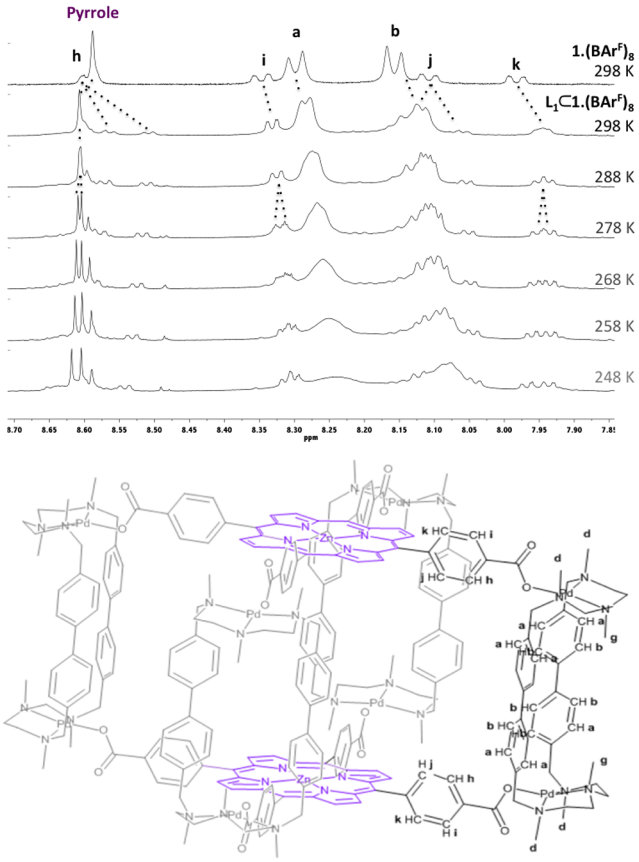

Figure 4. Partial ^{1}H NMR spectra (CD_3CN, 600 MHz) of $\mathbf{1}\cdot(\mathbf{BAr^F})_8$ at 298 K and temperature dependence of the ^{1}H NMR spectra of $\mathbf{L_1}\subset\mathbf{1}\cdot(\mathbf{BAr^F})_8$. Pyrrole protons appear in violet.

tetragonal prismatic cage $\mathbf{1}\cdot(\mathbf{BAr^F})_8$. Indeed, the resulting host–guest complex is nonsymmetrical, with respect to the north/south and east/west faces. In theory, four pyrrole peaks should be observed. In practice, only two pyrrole signals of the same intensity (north/south) were observed in the low-temperature NMR experiments, indicating a fast rotation of $\mathbf{L_1}$ within $\mathbf{1}\cdot(\mathbf{BAr^F})_8$ between four equivalent conformations (C_4 symmetry along the Zn–bpy–Zn axis). Remarkably, all protons of the encapsulated $\mathbf{L_1}$ display well-defined ^{1}H signals (at 298 and 243 K in CD_3CN), indicating that the confined ligand remains symmetric. The retention of the encapsulated $\mathbf{L_1}$ symmetry reveals a fast dynamic behavior, even at a low temperature (Figure S14). $\mathbf{L_1}$ rotation within $\mathbf{1}\cdot(\mathbf{BAr^F})_8$ was very fast on the NMR time scale, even at 243 K, so that activation parameters for guest rotation could not be determined. This behavior strongly contrasts with the reported encapsulation of the polypyridine guests (*S*)-***α***,[24] and **(m-Py)exTTF**,[25] which exhibit single signals and very broad set of signals at 298 K, and two set of signals at 243 K, revealing steric clashes between host and guest, leading to a complex dynamic process at 298 K and the loss of the guest symmetry at 243 K.

The large binding constant value calculated for $\mathbf{L_1}\subset\mathbf{1}\cdot(\mathbf{BAr^F})_8$ ($K_a = (1.6 \pm 0.3) \times 10^6\ M^{-1}$), together with the loss of the cage symmetry (north/south) observed upon encapsulation of $\mathbf{L_1}$, indicate that no dissociation/re-encapsulation processes occur on the NMR time scale, the guest orientation being maintained in $\mathbf{L_1}\subset\mathbf{1}\cdot(\mathbf{BAr^F})_8$. This is supported by the DOSY ^{1}H NMR experiments of a mixture of $\mathbf{1}\cdot(\mathbf{BAr^F})_8$ and $\mathbf{L_1}$ that clearly show that the encapsulated $\mathbf{L_1}$ signals exhibits the same diffusion value than the host cage (hydrodynamic ratio of 18.5 Å; see Spectra S7 in the Supporting Information).

Preparation of the Encapsulated Zn^{II}, Cu^{II} and Fe^{III} Complexes of $\mathbf{L_1}\subset\mathbf{1}\cdot(\mathbf{BAr^F})_8$. Host–guest adducts of general formula $\mathbf{L_1Zn^{II}(Cl)_2}\subset\mathbf{1}\cdot(\mathbf{BAr^F})_8$, $\mathbf{L_1Cu^{II}(Br)_2}\subset\mathbf{1}\cdot(\mathbf{BAr^F})_8$ and $\mathbf{L_1Fe^{III}(Cl)_3}\subset\mathbf{1}\cdot(\mathbf{BAr^F})_8$ were prepared by reacting $\mathbf{L_1}\subset\mathbf{1}\cdot(\mathbf{BAr^F})_8$ with stoichiometric amounts of $ZnCl_2$, $CuBr_2$, and $FeCl_3$ in CH_3CN at room temperature.[30] Upon 15 min of stirring, the targeted compounds were isolated after crystallization by slow diffusion of diethyl ether. The resulting host–guest adducts were characterized by means of 1D and 2D ^{1}H NMR spectroscopy, as well as by EPR in the case of the paramagnetic Cu^{II} complex.

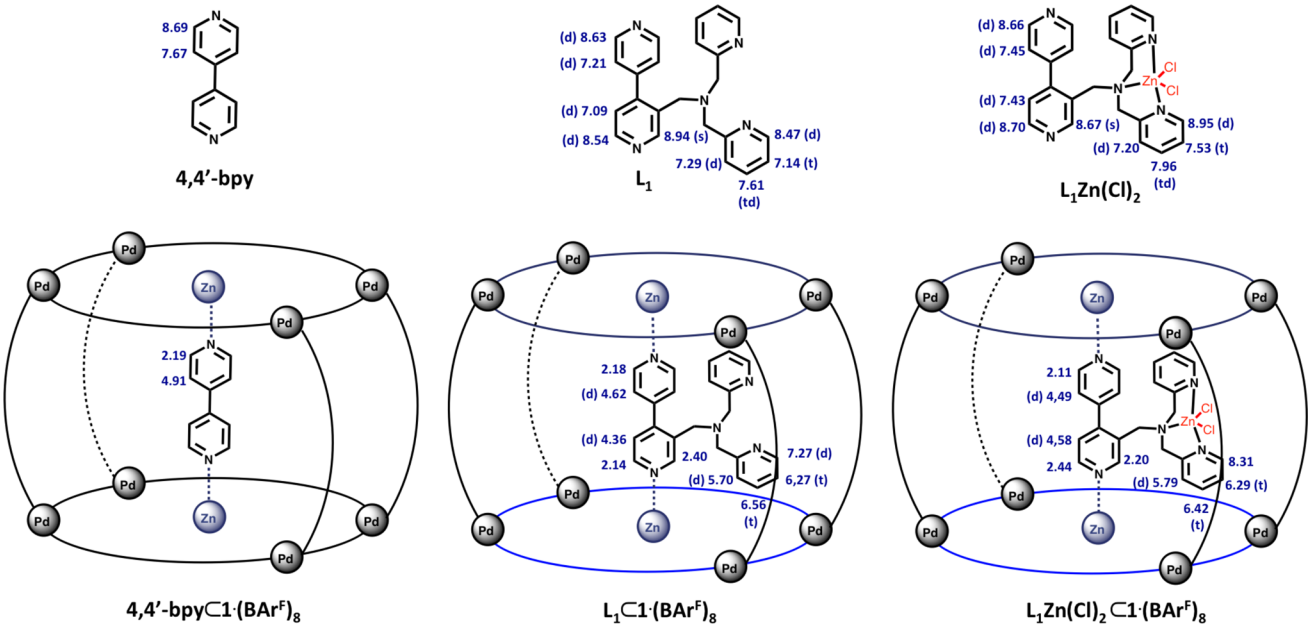

Figure 5. ^{1}H NMR (CD_3CN, 400 MHz, room temperature) assignment of free and encapsulated **4,4′-bpy**,[24] $\mathbf{L_1}$, and $\mathbf{L_1Zn(Cl)_2}$ (this study).

DOI: 10.1021/acs.inorgchem.7b02852
Inorg. Chem. 2018, 57, 3529–3539

By comparison with $\mathbf{L_1{\subset}1{\cdot}(BAr^F)_8}$, the ^{1}H NMR spectrum of the encapsulated Zn-complex $\mathbf{L_1Zn^{II}(Cl)_2{\subset}1{\cdot}(BAr^F)_8}$ displays a new set of signals (Figure S15 in the Supporting Information), which can be assigned to the aromatic protons of the confined $\mathbf{L_1Zn^{II}(Cl)_2}$ from the evident COSY cross-peaks and analysis of the HSQC spectra (see Figures S16 and S17 in the Supporting Information). Compared to $\mathbf{L_1{\subset}1{\cdot}(BAr^F)_8}$, the signals corresponding to $\mathbf{L_1}$ are slightly shifted in $\mathbf{L_1Zn^{II}(Cl)_2{\subset}1{\cdot}(BAr^F)_8}$ with a strong downfield shift occurring on the protons at the α-position of the two pendent pyridines of the **BPA** moiety (resonating at 8.31 ppm), which remain equivalent (see Figures 5 and 6a).

Compared to the free $\mathbf{L_1Zn^{II}(Cl)_2}$ complex (see Figure 5, as well as Figures S4 and S5), the signals corresponding to the **4,4′-bpy** and the **BPA** moiety in $\mathbf{L_1Zn^{II}(Cl)_2{\subset}1{\cdot}(BAr^F)_8}$ are experiencing a strong and a moderate upfield shift, respectively. This difference in the shifting strength unambiguously confirms the encapsulation of the Zn^{II} complex within $\mathbf{1{\cdot}(BAr^F)_8}$) through the simultaneous interaction of its **4,4′-bpy** anchor with the two Zn-porphyrins units. DOSY-NMR experiments also support the encapsulation, since signals of the encapsulated complex $\mathbf{L_1Zn^{II}(Cl)_2}$ present the same diffusion coefficient as the cage (Spectra S8 in the Supporting Information). The ^{1}H NMR spectrum of $\mathbf{L_1Zn^{II}(Cl)_2{\subset}1{\cdot}(BAr^F)_8}$ at room temperature displayed two separated singlets at 8.66 and 8.84 ppm, assigned to the nonsymmetrical pyrrole protons of the two Zn-porphyrins (north and south) of $\mathbf{1{\cdot}(BAr^F)_8}$ (Figure S15). Furthermore, all aromatic protons of the encapsulated $\mathbf{L_1Zn^{II}(Cl)_2}$ complex display well-defined ^{1}H signals at 298 K in CD_3CN, indicating that the methylpyridine arms in confined complex remain symmetrically equivalent (Figure 6a). Thus, similar to $\mathbf{L_1{\subset}1{\cdot}(BAr^F)_8}$, a fast rotation of $\mathbf{L_1Zn^{II}(Cl)_2}$ in $\mathbf{1{\cdot}(BAr^F)_8}$ around the Zn−bpy-Zn axis is observed, and no apparent steric clashes exist between host and guest upon formation of the metallo-complex.

Variable-temperature ^{1}H NMR studies reveals a line-broadening effect at low temperature (248 K) on the signals at 6.42, 6.29, and 5.79 ppm corresponding to the pyridine protons of the **BPA** moiety of $\mathbf{L_1}$, while aromatic protons of the **bpy** unit (4.58 and 4.49 ppm) kept resonating as sharp signals (Figure 6b). The spatial proximity between $\mathbf{L_1}$ and cage protons was also confirmed by NOESY contacts (Figure S18 in the Supporting Information). Lowering the flexibility of the **BPA**-pyridine units upon decreasing the temperature can explain such behavior. However, the fast rotation of $\mathbf{L_1Zn^{II}(Cl)_2}$ along the Zn−Zn axis is maintained at 248 K (retention of the symmetry east/west; see Figure S19 in the Supporting Information).

The ^{1}H NMR spectrum of the $\mathbf{L_1Cu^{II}(Br)_2{\subset}1{\cdot}(BAr^F)_8}$ host−guest complex at room temperature displayed key indicative features of metal coordination to $\mathbf{L_1{\subset}1{\cdot}(BAr^F)_8}$; most obvious is a strong line broadening due to paramagnetism of the signal corresponding to the pyrrole protons of the zinc porphyrin, illustrating a loss of the cage symmetry north/south (see Figure S20 in the Supporting Information). The ^{1}H NMR spectrum of $\mathbf{L_1Fe^{III}(Cl)_3{\subset}1{\cdot}(BAr^F)_8}$ at room temperature also displayed a strong splitting of the signal of the pyrrole protons of the two Zn-porphyrin units, which resonate at 8.62 and 8.60 ppm (Figure S22 in the Supporting Information). The signal corresponding to the protons of the **BPA** moiety of $\mathbf{L_1}$ can no longer be detected, indicating the coordination of the paramagnetic Cu^{II} and Fe^{III} cations. Interestingly, in the case of $\mathbf{L_1Cu^{II}(Br)_2{\subset}1{\cdot}(BAr^F)_8}$, resonances at 4.76 and 4.72 ppm with 2D COSY crossed peaks at 2.25 and 2.47 ppm, respectively, were attributed to the **4,4′-bpy** moiety (see Figure S21).

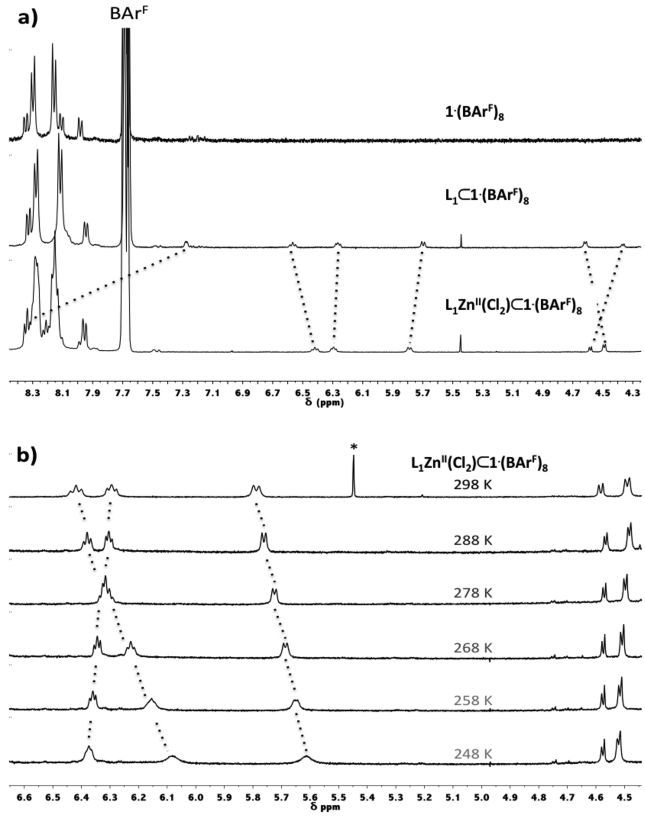

Figure 6. (a) ^{1}H NMR spectra (CD_3CN, 400 MHz) of $\mathbf{1{\cdot}(BAr^F)_8}$, $\mathbf{L_1{\subset}1{\cdot}(BAr^F)_8}$ and $\mathbf{L_1Zn^{II}(Cl)_2{\subset}1{\cdot}(BAr^F)_8}$ at 298 K (depicted region 4.2−8.4 ppm). (b) Temperature dependence of the ^{1}H NMR spectra (CD_3CN, 600 MHz) of $\mathbf{L_1Zn^{II}(Cl)_2{\subset}1{\cdot}(BAr^F)_8}$ (enlarged region: 4.5−6.5 ppm). Peak labeled with an asterisk (*) corresponds to CH_2Cl_2.

The confined paramagnetic Cu^{II} center was further studied by recording EPR spectra of $\mathbf{L_1Cu^{II}(Br)_2}$ and $\mathbf{L_1Cu^{II}(Br)_2{\subset}1{\cdot}(BAr^F)_8}$ at 77 K. The EPR spectra of $\mathbf{L_1Cu^{II}(Br)_2}$ and $\mathbf{L_1Cu^{II}(Br)_2{\subset}1{\cdot}(BAr^F)_8}$ in acetonitrile are clearly distinct, illustrating the selective confinement of the Cu^{II} complex in $\mathbf{1{\cdot}(BAr^F)_8}$ (Figure 7). For the free $\mathbf{L_1Cu^{II}(Br)_2}$ complex, only a broad isotropic signal, characteristic of **BPA**-based CuN_3Br_2 and CuN_3Cl_2 complexes, was observed (Figure 7a).[31−33] This signal broadening can be explained by intermolecular metal ion spin−spin interactions.[34] The EPR spectrum of $\mathbf{L_1Cu^{II}(Br)_2}$ recorded in butyronitrile, a solvent with a lower dielectric constant, which is expected to minimize magnetic interactions between Cu centers,[33,35] instead gave a well-resolved axial Cu^{II} signal (Figure 7b), further supporting this assumption. Importantly, the EPR spectrum of $\mathbf{L_1Cu^{II}(Br)_2{\subset}1{\cdot}(BAr^F)_8}$ in CH_3CN is markedly different (Figure 7c); it shows an axial anisotropy with a rhombic distortion. A very similar EPR spectrum is obtained for $\mathbf{L_1Cu^{II}(Br)_2{\subset}1{\cdot}(BAr^F)_8}$ in butyronitrile (Figure 7d), indicating the presence of similar coordination environments inside the cage, irrespective of the solvent (Note: Red lines in Figure 7 represent simulations determined by using the parameters given in Table 1).

Therefore, cage $\mathbf{1{\cdot}(BAr^F)_8}$ clearly acts as a second coordination sphere preventing magnetic communication between the Cu complexes. Similar observations (well-resolved axial anisotropic signal) have been reported by the attachment of bulky bioconjugates to **BPA**-based Cu^{II} complexes, which prevent intermolecular Cu−Cu spin−spin interactions.[31,31] The gain of

DOI: 10.1021/acs.inorgchem.7b02852
Inorg. Chem. 2018, 57, 3529−3539

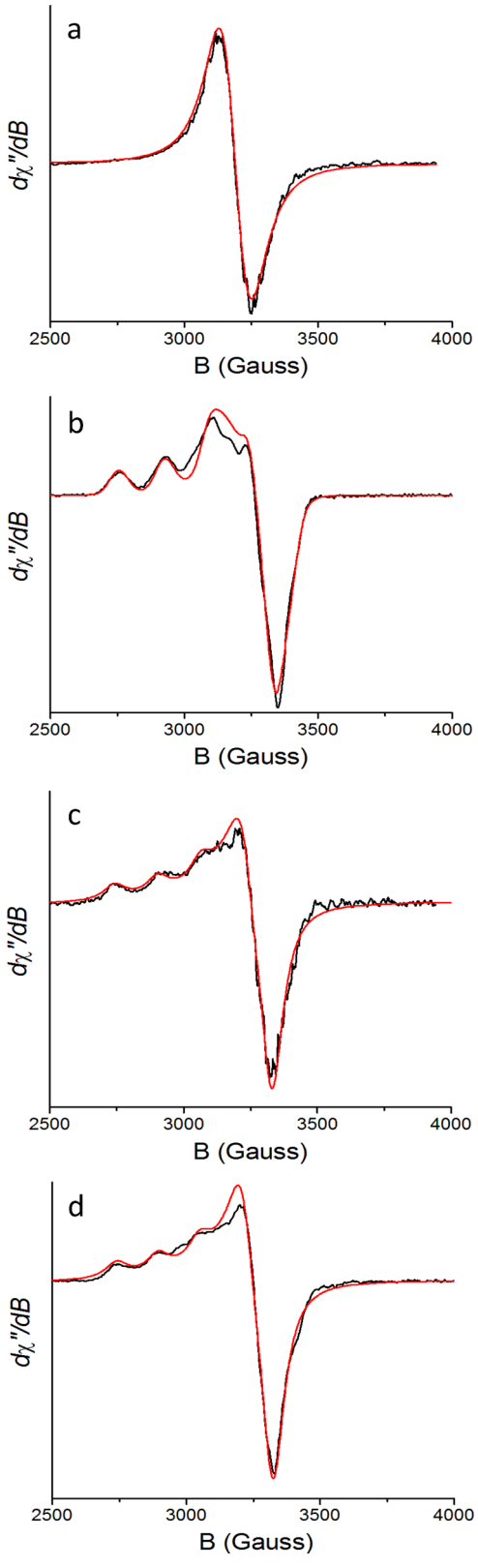

Figure 7. EPR spectra at 77 K of $L_1Cu^{II}(Br)_2$ (0.5 mM) in (a) acetonitrile and (b) butyronitrile and of $L_1Cu^{II}(Br)_2\subset 1\cdot(BAr^F)_8$ (0.5 mM) in (c) acetonitrile and (d) butyronitrile. Solid black lines represent the experimental spectra and red lines are simulations by using the parameters given in Table 1.

anisotropy of a cobalt-porphyrin derivative upon its encapsulation in a supramolecular cage also has been reported.[23c]

Solid-State Coordination of Zn^{II}, Cu^{II}, and Fe^{III} for Preparation of Complexes of $L_1\subset 1\cdot(BAr^F)_8$. Taking advantage of the orthogonal solubility in Et_2O between $L_1\subset 1\cdot(BAr^F)_8$ (insoluble) and the $ZnCl_2$, $CuBr_2$ and $FeCl_3$ salts (soluble), we explored the possibility of performing solid-phase coordination of the neutral salts using $L_1\subset 1\cdot(BAr^F)_8$. Performing solid-state chemistry within a well-defined molecular cage is particularly challenging, since the close packing of molecular cages in the solid state often prevents guest entry.[36] However, in light of (i) the remarkable spongelike behavior of the cage $1\cdot(BAr^F)_8$, which can perform solid-phase fullerene encapsulation,[37] and (ii) the fast motion of the encapsulated L_1, observed at low temperature (243 K), $L_1\subset 1\cdot(BAr^F)_8$ can be considered as a good candidate toward solid-phase coordination chemistry in a molecular cage. Few crystals of the $L_1\subset 1\cdot(BAr^F)_8$ host–guest adduct were soaked in a solution of $ZnCl_2$, $FeCl_3$ in Et_2O, or $CuBr_2$ in a Et_2O/CH_3OH 99:1 solvent mixture (15 mM, ~20 equiv) and slowly stirred for 15 min. In the case of $CuBr_2$ and $FeCl_3$, the color of the crystals rapidly turned from bright pink to dark purple (Figure S23 in the Supporting Information). The resulting crystalline materials were then washed thoroughly with neat Et_2O (20 h of stirring), evaporated to dryness, and dissolved in CH_3CN. ESI-HRMS analysis unambiguously supported the formation of $L_1Zn^{II}(Cl)_2\subset 1\cdot(BAr^F)_8$ (see Figure 8, as well as Figure S24 in the Supporting Information), $L_1Cu^{II}(Br)_2\subset 1\cdot(BAr^F)_8$ (Figure S26 in the Supporting Information) and $L_1Fe^{III}(Cl)_3\subset 1\cdot(BAr^F)_8$ (see Figure 9, as well as Figure S27 in the Supporting Information) in a 1:1 stoichiometry. Zn-, Cu-, and Fe-coordination by the encapsulated ligand in $L_1\subset 1\cdot(BAr^F)_8$ was further confirmed by tandem MS/MS analysis.

When the mass-selected $[L_1Zn^{II}(Cl)_2\subset 1\cdot(BAr^F)_1]^{7+}$ complex (m/z = 929.5; 7+) was subjected to CID, isotopic patterns corresponding to the empty $[1\cdot(BAr^F)_1\cdot Cl]^{6+}$ (m/z = 1006.4; 6+), and the Zn-complex $[L_1Zn^{II}Cl]^+$ (m/z = 466.1; 1+) were observed; a collision energy of 15 eV was needed to observe a total dissociation (see Figure S25). This collision energy is similar to that needed for the total dissociation of $L_1\subset 1\cdot(BAr^F)_8$, indicating similar interaction strength (Figure S9).

CID of the mass-selected $[L_1Cu^{II}(Br)_2\subset 1\cdot(BAr^F)_1]^{7+}$ complex (m/z = 941.9; 7+) gave an isotopic pattern corresponding to the empty $[1\cdot(BAr^F)_1\cdot Br]^{6+}$ (m/z = 1013.5; 6+) and the Cu complex $[L_1Cu^{II}Br]^+$ (m/z = 511.0; 1+); a collision energy of 10 eV was needed to observed a total dissociation (Figure S27). In the case of the iron complex, a collision energy of 10 eV was also needed to observe a total dissociation of the mass-selected $[L_1Fe(Cl)_3\subset 1]^{8+}$ (m/z = 708.7; 8+), leading to an isotopic pattern corresponding to the empty $[1\cdot Cl]^{7+}$ (m/z = 739.3; 7+), and $[L_1Fe^{III}(Cl)_2]^+$ (m/z = 493.0; 1+) (Figure 9). These collision energies are lower than that needed for the total dissociation of $L_1\subset 1\cdot(BAr^F)_8$ (15 eV) indicating a weaker interaction in the gas phase for the Cu^{II} and Fe^{III}-based guests.

Host–Guest Studies by UV-vis Titration and Fluorescence Quenching Studies. The effect of the encapsulation of metallo-complexes over the absorption and emission properties of the cage $1\cdot(BAr^F)_8$ was studied through UV-vis titration and fluorescence measurements. As observed in their X-ray structure, the **4,4′-bpy** unit of $L_1Cu^{II}(Br)_2$ and $L_1Fe^{III}(Cl)_3$ remains available for coordination. Therefore, UV-vis titration experiments between the nanocapsule and these free-diffusing complexes have been performed in order to determine the association constant values. UV-vis titrations experiments of the host–guest interaction between $1\cdot(BAr^F)_8$ and $L_1Cu^{II}(Br)_2$ or $L_1Fe^{III}(Cl)_3$, indicate the formation of the

DOI: 10.1021/acs.inorgchem.7b02852
Inorg. Chem. 2018, 57, 3529–3539

Table 1. EPR Spin Hamiltonian Parameters of $L_1Cu^{II}(Br)_2$ and $L_1Cu^{II}(Br)_2\subset 1\cdot(BAr^F)_8$ Extracted from Simulations[a]

sample	solvent	g_x	g_y	g_z	A_{II}
$L_1Cu^{II}(Br)_2$	acetonitrile	2.10			
$L_1Cu^{II}(Br)_2$	butyronitrile	2.06	2.07	2.23	172
$L_1Cu^{II}(Br)_2\subset 1\cdot(BAr^F)_8$	acetonitrile	2.05	2.07	2.25	161
$L_1Cu^{II}(Br)_2\subset 1\cdot(BAr^F)_8$	butyronitrile	2.05	2.07	2.26	154

[a]Hyperfine values are given in Gauss.

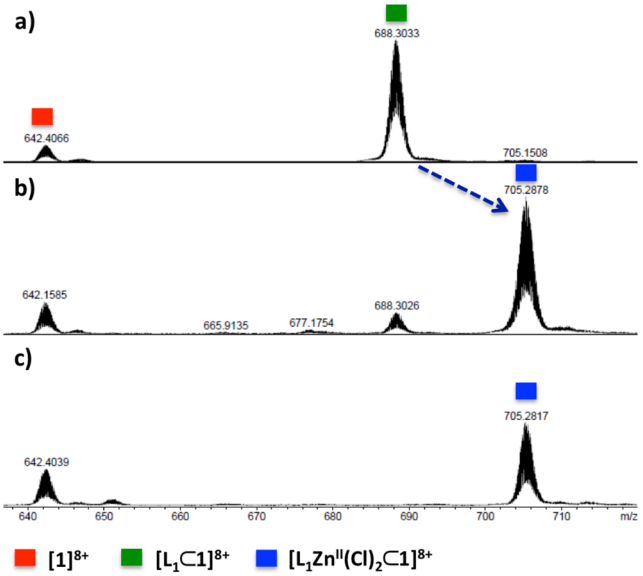

Figure 8. (a) ESI-HRMS spectra of $L_1\subset 1\cdot(BAr^F)_8$. (b) ESI-HRMS monitoring of the formation of $L_1Zn^{II}(Cl)_2\subset 1\cdot(BAr^F)_8$ in solution through the reaction of stoichiometric amounts of $ZnCl_2$ in CH_3CN at room temperature. (c) ESI-HRMS monitoring of the formation of $L_1Zn^{II}(Cl)_2\subset 1\cdot(BAr^F)_8$ by Zn-coordination in solid state by soaking crystals of $L_1\subset 1\cdot(BAr^F)_8$ in a solution of $ZnCl_2$ in Et_2O at room temperature.

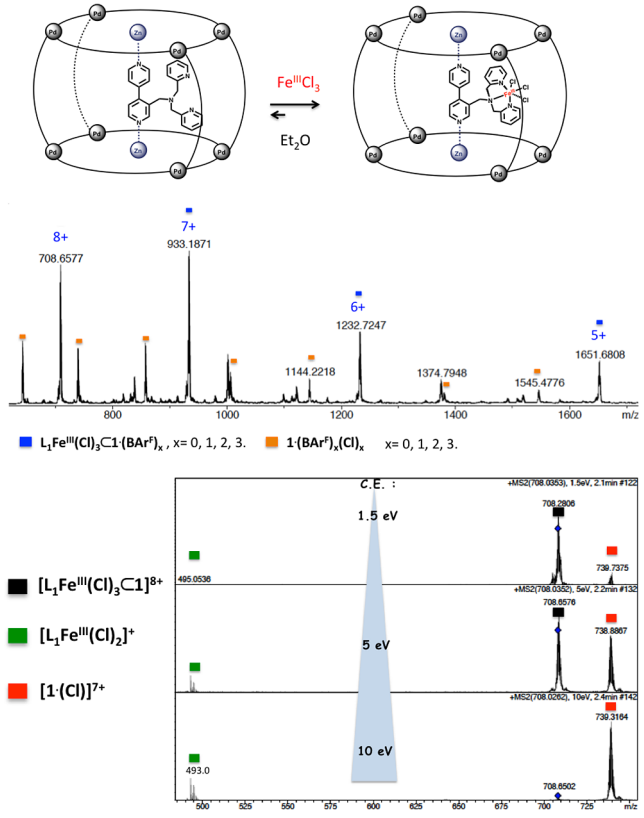

Figure 9. ESI-HRMS spectra of $L_1Fe^{III}(Cl)_3\subset 1\cdot(BAr^F)_x$ (top). ESI-MS-MS analysis of the collision-induced dissociation (CID) of $[L_1Fe^{III}(Cl)_3\subset 1]^{8+}$ host–guest complex (m/z = 708.7; 8+) (bottom).

$L_1Cu^{II}(Br)_2\subset 1\cdot(BAr^F)_8$ and $L_1Fe^{III}(Cl)_3\subset 1\cdot(BAr^F)_8$ adducts in a 1:1 stoichiometry (Job plot; see Figures S27 and S29 in the Supporting Information). Both UV-vis titrations display bathochromic shifts of the Soret band from the porphyrin units (Figure 10), exhibiting isosbestic points. Calculations based on the Soret shift result in binding constants of $K_a = (1.77 \pm 0.09) \times 10^5\ M^{-1}$ and $K_a = (1.42 \pm 0.06) \times 10^5\ M^{-1}$ for $L_1Cu^{II}(Br)_2$ and $L_1Fe^{III}(Cl)_3$, respectively. These binding constants are one order of magnitude lower, compared to L_1 ($(1.59 \pm 0.19) \times 10^6\ M^{-1}$), being in good agreement with the weaker interaction observed in the gas phase (tandem MS/MS experiments) for both Cu^{II}- and Fe^{III}-based guests.

Host–Guest Fluorescence Quenching Studies. Several transition-metal complexes (Ni^{II}, Cu^{II}, Ag^{II}) are reported in the literature as moderate to excellent excited-state quenchers.[38] In particular, paramagnetic metal ions have been shown to increase the quenching efficiency. The porphyrin photoexcited singlet state was shown to be quenched through an intramolecular photoinduced energy transfer process.[39] These observations have led to the construction of fluorescent metal ion chemosensors based on porphyrin analogues, through the development of porphyrin-metal receptor dyads.[40,41] Terpyridine, bipicolylamine, or 2,2′-dipyridylamine receptors covalently linked to the periphery of porphyrin derivatives have been widely used as efficient metal ion chemosensors.[42] On this basis, we explored the possibility of a guest-induced quenching of the metalloporphyrin-based fluorescence of $1\cdot(BAr^F)_8$ upon formation of the host–guest adducts involving paramagnetic metals, such as in $L_1Cu^{II}(Br)_2\subset 1\cdot(BAr^F)_8$ and $L_1Fe^{III}(Cl)_3\subset 1\cdot(BAr^F)_8$.

The fluorescence spectra of the cage $1\cdot(BAr^F)_8$ ($2 \times 10^6\ M^{-1}$) upon the addition of 2.0 equiv of L_1, $L_1Cu^{II}(Br)_2$, or $L_1Fe^{III}(Cl)_3$,[43] were recorded in a CH_2Cl_2/CH_3CN 9:1 solvent mixture (Figure 11). Fluorescence areas of 180 000, 416 000, 101 000, and 74 000 were found for $1\cdot(BAr^F)_8$, $L_1\subset 1\cdot(BAr^F)_8$, $L_1Cu^{II}(Br)_2\subset 1\cdot(BAr^F)_8$, and $L_1Fe^{III}(Cl)_3\subset 1\cdot(BAr^F)_8$, respectively. An increase in the fluorescence intensity (by a factor of 2.3) is observed when L_1 is bound within $1\cdot(BAr^F)_8$. This behavior can be explained by the well-described pyridine axial binding to Zn-porphyrin derivatives, which increase the absorption intensity (Q-bands) and therefore leads to improved photosensitizing properties.[44] Interestingly, a clear quenching of fluorescence upon encapsulation of paramagnetic complexes is observed. The fluorescence intensity of $L_1Cu^{II}(Br)_2\subset 1\cdot(BAr^F)_8$ is 1.8 times lower than $1\cdot(BAr^F)_8$ and 4.1 times lower than $L_1\subset 1\cdot(BAr^F)_8$. A similar effect is observed for $L_1Fe^{III}(Cl)_3\subset 1\cdot(BAr^F)_8$ with a fluorescence intensity that is, respectively, 2.4 and 5.6 times lower than that of $1\cdot(BAr^F)_8$ and $L_1\subset 1\cdot(BAr^F)_8$. Therefore, the markedly different fluorescence observed upon encapsulation of

DOI: 10.1021/acs.inorgchem.7b02852
Inorg. Chem. 2018, 57, 3529–3539

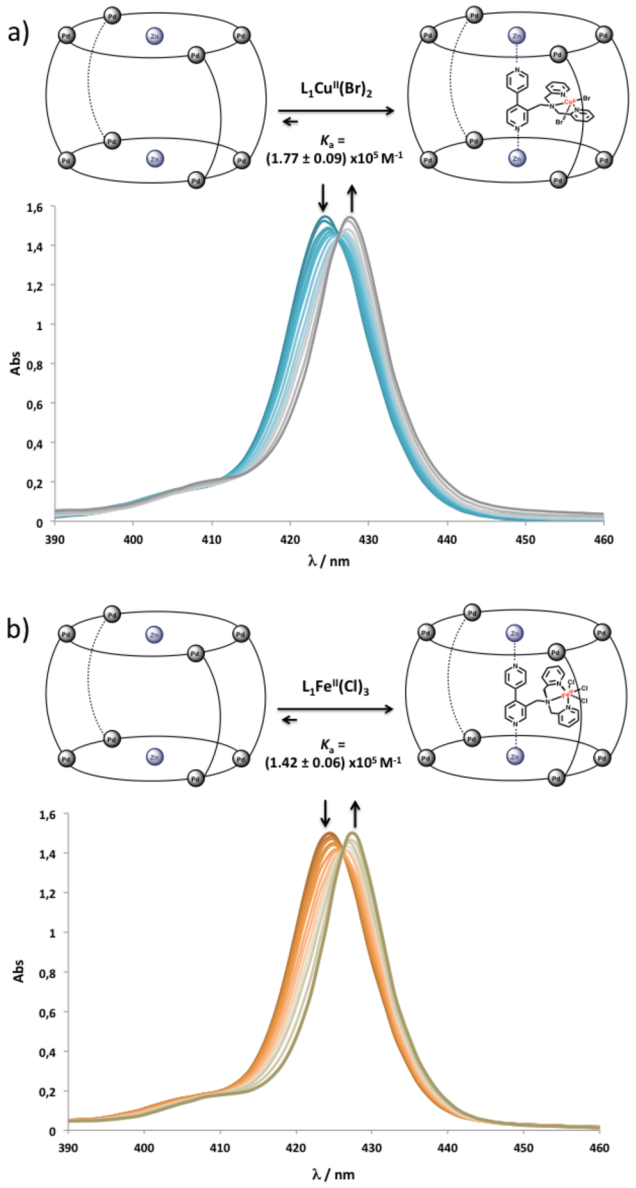

Figure 10. UV-vis monitoring of the titration of the nanocapsule $\mathbf{1}\cdot(\mathbf{BAr^F})_8$, with (a) $\mathbf{L_1Cu^{II}(Br)_2}$ and (b) $\mathbf{L_1Fe^{III}(Cl)_3}$, at a fixed total concentration (1.12×10^{-6} M) of $\mathbf{1}\cdot(\mathbf{BAr^F})_8$ in a toluene/CH_3CN solvent mixture (9:1), together with the calculated binding constants (K_a). In both cases, the final absorbance spectra are corresponding to the addition of 2.0 equiv of guest.

$\mathbf{L_1}$ (increase) or paramagnetic metallo-complexes (quenching) confirms the expected guest-dependent emission properties of the host $\mathbf{1}\cdot(\mathbf{BAr^F})_8$.

CONCLUSION

In summary, we have shown that nanocapsule $\mathbf{1}\cdot(\mathbf{BAr^F})_8$ can be used as a second coordination sphere model for the encapsulation of metallocomplexes. The functional duality of the designed ligand $\mathbf{L_1}$ allows for a strong anchoring into the cage $\mathbf{1}\cdot(\mathbf{BAr^F})_8$, along with the simultaneous coordination of Zn^{II}, Cu^{II}, and Fe^{III} metal ions, resulting in metallocomplexes entrapped in the well-defined cavity of $\mathbf{1}\cdot(\mathbf{BAr^F})_8$. ^1H NMR studies of $\mathbf{L_1}$ and $\mathbf{L_1Zn^{II}(Cl)_2}\subset\mathbf{1}$ allow for a remarkable characterization of the metal coordination in the confined space. This behavior strongly differs from previously reported polypyridine guests binding $\mathbf{1}\cdot(\mathbf{BAr^F})_8$, which were displaying broad and ill-defined NMR

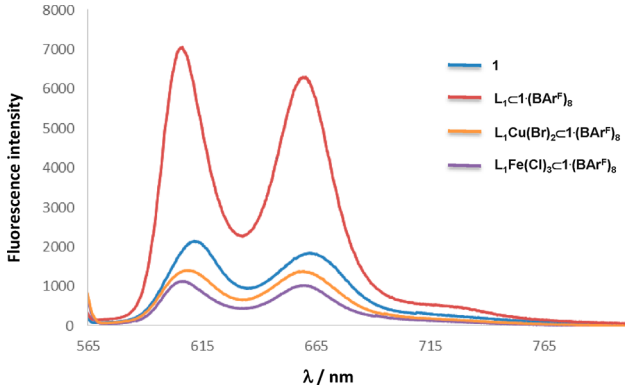

Figure 11. Superimposed fluorescence emission spectra of $\mathbf{1}\cdot(\mathbf{BAr^F})_8$ (blue), and $\mathbf{1}\cdot(\mathbf{BAr^F})_8$ in the presence of two equivalents of $\mathbf{L_1}$ ($\mathbf{L_1}\mathbf{1}\cdot(\mathbf{BAr^F})_8$, red), $\mathbf{L_1Cu^{II}(Br)_2}$ ($\mathbf{L_1Cu^{II}(Br)_2}\mathbf{1}\cdot(\mathbf{BAr^F})_8$, yellow) and $(\mathbf{L_1Fe^{III}(Cl)_3}(\mathbf{L_1Fe^{III}(Cl)_3}\mathbf{1}\cdot(\mathbf{BAr^F})_8$, purple).

spectra, presumably due to steric clashes between the complex and the nanocage, which limit the dynamic properties. Importantly, the synthesis of confined metallocomplexes inside the nanovessel $\mathbf{1}\cdot(\mathbf{BAr^F})_8$, was both achieved by coordination chemistry in solution, as well as in the solid-state by soaking of $\mathbf{L_1}\subset\mathbf{1}\cdot(\mathbf{BAr^F})_8$ in ethereal solutions of the metal salts ($ZnCl_2$, $CuBr_2$, and $FeCl_3$). The development of well-defined nanoreactors, which can be used in both homogeneous or heterogeneous fashion, opens the door to the exploration of functional models merging the high efficiency and recyclability found in heterogeneous catalysis with the convenient characterization of homogeneous systems.

The prism $\mathbf{1}\cdot(\mathbf{BAr^F})_8$ displays two cofacial Zn-porphyrin fluorophores. We have demonstrated that the fluorescence emission of $\mathbf{1}\cdot(\mathbf{BAr^F})_8$ is strongly influenced by the encapsulation of a guest. Indeed, the binding of the neutral $\mathbf{L_1}$ increased the fluorescence intensity by a factor of 2.3, whereas the inclusion of the paramagnetic complexes $\mathbf{L_1Cu^{II}(Br)_2}$ and $\mathbf{L_1Fe^{III}(Cl)_3}$ resulted in a pronounced fluorescence quenching, representing a remarkable example of fluorescent metal-ion sensor based on host–guest interactions.

Overall, the host–guest complexes here reported are proof of concept of the ability of self-assembled nanocages, containing tunable metalloporphyrins and macrocyclic molecular clips, to host bioinspired metallocomplexes and confer upon them a second sphere coordination that isolates and protects them, thus opening the possibility to study the intrinsic reactivity of bioinspired species at the confined space. We are currently interested in the study of the behavior of confined redox-active Cu^I and Fe^{II} bioinspired complexes.

EXPERIMENTAL SECTION

Synthesis of 4,4′-bpy(Ald). 4,4′-bipyridine-2-carboxaldehyde was obtained in a 30% yield by following a reported protocol.[16]

Synthesis of Ligand $\mathbf{L_1}$. 4,4′-Bipyridine-2-carboxaldehyde (100 mg, 0.54 mmol, 1.0 equiv) was dissolved in anhydrous methanol (9.5 mL). Bis(2-pyridylmethyl)amine (**BPA**) (97 μL, 0.54 mmol, 1.0 equiv) and two drops of glacial acetic acid were then added to the mixture. The resulting mixture was refluxed for 30 min. The reaction mixture was cooled to 0 °C and sodium cyanoborohydride (68 mg, 1.08 mmol, 2.0 equiv) was slowly added under vigorous stirring. The mixture was then slowly warmed to room temperature and stirred overnight. Then 4 mL of H_2O and 6 mL of an aqueous Na_2CO_3 saturated solution were added to the mixture. The mixture was then extracted with dichloromethane (3 × 10 mL), dried over $MgSO_4$, filtered, and evaporated to dryness. The residue was purified by column chromatography

DOI: 10.1021/acs.inorgchem.7b02852
Inorg. Chem. 2018, 57, 3529–3539

on neutral alumina (eluent: hexane/EtOAc; 60:40 to EtOAc) to afford $\mathbf{L_1}$ as a yellow solid. Yield: 55%. ^{1}H NMR (400 MHz, $CDCl_3$) δ ppm: 8.94 (s, 1H, ArH), 8.63 (dd, 2H, ArH), 8.54 (d, 1H, ArH), 8.47 (dd, 2H, ArH), 7.61 (td, 2H, ArH), 7.29 (d, 2H, ArH), 7.21 (dd, 2H, ArH), 7.14 (t, 2H, ArH), 7.09 (d, 1H, ArH), 3.73 (s, 2H, bpy-CH_2^-), 3.68 (s, 4H, (py-CH_2^-)$_2$). HRMS (ESI, $[M + H]^+$): m/z calcd for $C_{23}H_{21}N_5H$ 368.1870, found 368.71. HRMS (ESI, $[M + Na]^+$): m/z calcd for $C_{23}H_{21}N_5Na$ 390.1689, found 390.1698.

Synthesis of $\mathbf{L_1Zn^{II}(Cl)_2}$. A solution of $ZnCl_2$ (9 mg, 0.066 mmol, 1.01 equiv) in MeOH (1 mL) was added at room temperature to a stirred solution of $\mathbf{L_1}$ (24 mg, 0.065 mmol, 1.0 equiv) in MeOH (1 mL). The mixture was stirred at room temperature and, within 1 min, a white precipitate formed. The reaction was allowed to continue for 30 min. The white precipitate was collected by filtration through a frit, washed with a small amount of methanol and dried in vacuo to give $\mathbf{L_1Zn^{II}(Cl)_2}$ in a 56% yield. ^{1}H NMR (400 MHz, $CDCl_3$) δ ppm: 8.95 (d, 2H, ArH), 8.70 (d, 1H, ArH), 8.67 (s, 1H, ArH), 8.66 (d, 2H, ArH), 7.96 (td, 2H, ArH), 7.53 (t, 2H, ArH), 7.45 (d, 2H, ArH), 7.43 (d, 1H, ArH), 7.20 (d, 2H, ArH), 4.07 (s, 2H, bpy-CH_2^-), 3.82 (s, 4H, (py-CH_2^-)$_2$). HRMS (ESI, $[M - Cl]^+$): m/z calcd for $C_{23}H_{21}N_5ZnCl$ 466.0771, found 466.0923. (ESI, $[M + Na]^+$): m/z calcd for $C_{23}H_{21}N_5ZnCl_2Na$ 526.0329, found 526.0316.

Synthesis of $\mathbf{L_1Cu^{II}(Br)_2}$. A solution of $CuBr_2$ (12 mg, 0.054 mmol, 1.0 equiv) in CH_3CN (1.5 mL) was added at room temperature to a stirred solution of $\mathbf{L_1}$ (20 mg, 0.054 mmol, 1.0 equiv) in CH_3CN (1.5 mL). The mixture was stirred for 10 min and an excess of Et_2O was added. A green precipitate formed and was collected by filtration through a frit. Yield: 75%. Suitable crystals for X-ray analysis were obtained by vapor diffusion of Et_2O into a CH_3CN solution. HRMS (ESI, $[M - Br]^+$): m/z calcd for $C_{23}H_{21}N_5CuBr$ 511.0251, found 511.0293. HRMS (ESI, $[2\ M - Br]^+$): m/z calcd for $C_{46}H_{42}N_{10}Cu_2Br_3$ 1100.9691, found 1100.9752.

Synthesis of $\mathbf{L_1Fe^{III}(Cl)_3}$. A solution of $FeCl_3$ (14 mg, 0.086 mmol, 1.1 equiv) in THF (2 mL) was added at room temperature to a stirred solution of $\mathbf{L_1}$ (29 mg, 0.078 mmol, 1.0 equiv) in THF (2 mL). The mixture was stirred for 10 min and an excess of Et_2O was added. A yellow precipitate formed and was collected by filtration through a frit. Yield: 82%. Suitable crystals for X-ray analysis were obtained by vapor diffusion of Et_2O into a CH_3CN solution. HRMS (ESI, $[M - Cl]^+$): m/z calcd for $C_{23}H_{21}N_5FeCl_2$ 493.0519, found 493.0528. (ESI, $[M + Na]^+$): m/z calcd for $C_{23}H_{21}N_5FeCl_3Na$ 551.0105, found 551.0113.

Preparation of $\mathbf{L_1}\subset\mathbf{1}$. Nine milligrams (9 mg) of the nanocapsule $\mathbf{1}\cdot(\mathbf{BAr^F})_8$ (0.75 μmol, 1 equiv) were dissolved in 600 μL of CH_3CN. Then 1 equiv of $\mathbf{L_1}$ dissolved in CH_2Cl_2 (3.23×10^{-4} M) was added. The mixture was stirred at room temperature for 15 min, filtered through cotton, and recrystallized by diethyl ether diffusion. A quantitative yield was obtained. ESI-HRMS (m/z): Calcd 2239.9378, found 2239.6236 ($\{\mathbf{L_1}\subset\mathbf{1}\cdot(\mathbf{BAr^F})_4\}^{4+}$); Calcd 1619.1367, found 1619.1099 ($\{\mathbf{L_1}\subset\mathbf{1}\cdot(\mathbf{BAr^F})_3\}^{5+}$); Calcd 1205.4361, Found 1205.4260 ($\{\mathbf{L_1}\subset\mathbf{1}\cdot(\mathbf{BAr^F})_2\}^{6+}$); Calcd 909.9356, Found 909.9300 ($\{\mathbf{L_1}\subset\mathbf{1}\cdot(\mathbf{BAr^F})\}^{7+}$); Calcd 688.31, found 688.3069 ($\{\mathbf{L_1}\subset\mathbf{1}\}^{8+}$).

■ ASSOCIATED CONTENT

Supporting Information

The Supporting Information is available free of charge on the ACS Publications website at DOI: 10.1021/acs.inorgchem.7b02852.

Experimental procedure and compound characterization (PDF)

Accession Codes

CCDC 1582907−1582909 contain the supplementary crystallographic data for this paper. These data can be obtained free of charge via www.ccdc.cam.ac.uk/data_request/cif, or by emailing data_request@ccdc.cam.ac.uk, or by contacting The Cambridge Crystallographic Data Centre, 12 Union Road, Cambridge CB2 1EZ, U.K.; fax: +44 1223 336033.

■ AUTHOR INFORMATION

Corresponding Authors

*E-mail: miquel.costas@udg.edu (M. Costas).
*E-mail: xavi.ribas@udg.edu (X. Ribas).

ORCID

Vlad Martin-Diaconescu: 0000-0002-7575-2237
Teodor Parella: 0000-0002-1914-2709
Julio Lloret-Fillol: 0000-0001-9173-1105
Miquel Costas: 0000-0001-6326-8299
Xavi Ribas: 0000-0002-2850-4409

Notes

The authors declare no competing financial interest.

■ ACKNOWLEDGMENTS

We thank Spanish MINECO (Nos. CTQ2016-77989-P, CTQ2013-50306-EXP, and CTQ2015-64436-P), the Agence National de la Recherche (No. ANR-14-CE08-0001 JCJC BOMBER to S.G.), and the Generalitat de Catalunya (2014 SGR 862 and postdoctoral grant to C.C.), X.R. and M.C. are also grateful for ICREA-Acadèmia awards. We thank STR UdG for technical support.

■ REFERENCES

(1) Lippard, S. J.; Berg, J. M.; *Principles of Bioinorganic Chemistry*; University Science Books: Mill Valley, CA, 1994.

(2) (a) Solomon, E. I.; Sundaram, U. M.; Machonkin, T. E. Multicopper Oxidases and Oxygenases. *Chem. Rev.* **1996**, *96*, 2563−2605. (b) Ferguson-Miller, S.; Babcock, G. T. Heme/Copper Terminal Oxidases. *Chem. Rev.* **1996**, *96*, 2889−2907.

(3) Mann, S. I.; Heinisch, T.; Weitz, A. C.; Hendrich, M. P.; Ward, T. R.; Borovik, A. S. Modular Artificial Cupredoxins. *J. Am. Chem. Soc.* **2016**, *138*, 9073−9076.

(4) Korom, S.; Ballester, P. Attachment of a Ru^{II} complex to a self-folding hexaamide deep cavitand. *J. Am. Chem. Soc.* **2017**, *139*, 12109−12112.

(5) De Leener, G.; Over, D.; Smet, C.; Cornut, D.; Porras-Gutierrez, A. G.; Lopez, I.; Douziech, B.; Le Poul, N.; Topìc, F.; Rissanen, K.; Le Mest, Y.; Jabin, I.; Reinaud, O. "Two-Story" Calix[6]arene-Based Zinc and Copper Complexes: Structure, Properties, and O_2 Binding. *Inorg. Chem.* **2017**, *56*, 10971−10983.

(6) Perraud, O.; Sorokin, A. B.; Dutasta, J. P.; Martinez, A. Oxidation of cycloalkanes by H_2O_2 using a copper−hemicryptophane complex as a catalyst. *Chem. Commun.* **2013**, *49*, 1288−1290.

(7) Cohen, S. M.; Zhang, Z.; Boissonnault, J. A. Toward "metalloMOFzymes": Metal−Organic Frameworks with Single-Site Metal Catalysts for Small-Molecule Transformations. *Inorg. Chem.* **2016**, *55*, 7281−7290.

(8) Voloshin, Y.; Belaya, I.; Krämer, R. *The Encapsulation Phenomenon*; Springer International Publishing: Cham, Switzerland, 2016.

(9) Kawano, M.; Kobayashi, Y.; Ozeki, T.; Fujita, M. Direct Crystallographic Observation of a Coorditively Unsaturated Transition-Metal Complex in situ Generated within a Self-Assembled Cage. *J. Am. Chem. Soc.* **2006**, *128*, 6558−6559.

(10) Clever, G. H.; Kawamura, W.; Tashiro, S.; Shiro, M.; Shionoya, M. Stacked Platinum Complexes of the Magnus' Salt Type Inside a Coordination Cage. *Angew. Chem., Int. Ed.* **2012**, *51*, 2606−2609.

(11) Leung, D. H.; Bergman, R. G.; Raymond, K. N. Scope and Mechanism of the C-H Bond Activation Reactivity within a Supramolecular Host by an Iridium Guest: A Stepwise Ion Pair Guest Dissociation Mechanism. *J. Am. Chem. Soc.* **2006**, *128*, 9781−9797.

(12) Leung, D. H.; Bergman, R. G.; Raymond, K. N. Highly Selective Supramolecular Catalyzed Allylic Alcohol Isomerization. *J. Am. Chem. Soc.* **2007**, *129*, 2746−2747.

DOI: 10.1021/acs.inorgchem.7b02852
Inorg. Chem. 2018, 57, 3529−3539

(13) Fiedler, D.; Leung, D. H.; Bergman, R. G.; Raymond, K. N. Enantioselective Guest Binding and Dynamic Resolution of Cationic Ruthenium Complexes by a Chiral Metal-Ligand Assembly. *J. Am. Chem. Soc.* **2004**, *126*, 3674−3675.
(14) Kaphan, D. M.; Levin, M. D.; Bergman, R. G.; Raymond, K. N.; Toste, F. D. A Supramolecular Microenvironment Strategy for Transition Metal Catalysis. *Science* **2015**, *350*, 1235−1238.
(15) Cook, T. R.; Stang, P. J. Recent Developments in the Preparation and Chemistry of Metallacycles and Metallacages via Coordination. *Chem. Rev.* **2015**, *115*, 7001−7045.
(16) (a) De, S.; Pramanik, S.; Schmittel, M. A Toggle Nanoswitch Alternately Controlling Two Catalytic Reactions. *Angew. Chem., Int. Ed.* **2014**, *53*, 14255−14259. (b) Mittal, N.; Pramanik, S.; Paul, I.; De, S.; Schmittel, M. Networking Nanoswitches for ON/OFF Control of Catalysis. *J. Am. Chem. Soc.* **2017**, *139*, 4270−4273.
(17) Bar, A. K.; Mohapatra, S.; Zangrando, E.; Mukherjee, P. S. A Series of Trifacial Pd_6 Molecular Barrels with Porphyrin Walls. *Chem. - Eur. J.* **2012**, *18*, 9571−9579.
(18) Shi, Y.; Sanchez-Molina, I.; Cao, C.; Cook, T. R.; Stang, P. J. Synthesis and photophysical studies of self-assembled multicomponent supramolecular coordination prisms bearing porphyrin faces. *Proc. Natl. Acad. Sci. U. S. A.* **2014**, *111*, 9390−9395.
(19) Nakamura, T.; Ube, H.; Shiro, M.; Shionoya, M. A Self-Assembled Multiporphyrin Cage Complex through Three Different Zinc(II) Center Formation under Well-Balanced Aqueous Conditions. *Angew. Chem., Int. Ed.* **2013**, *52*, 720−723.
(20) Brenner, W.; Ronson, T. K.; Nitschke, J. R. Separation and Selective Formation of Fullerene Adducts within an $M^{II}_8L_6$ Cage. *J. Am. Chem. Soc.* **2017**, *139*, 75−78.
(21) Struch, N.; Bannwarth, C.; Ronson, T. K.; Lorenz, Y.; Mienert, B.; Wagner, N.; Engeser, M.; Bill, E.; Puttreddy, R.; Rissanen, K.; Beck, J.; Grimme, S.; Nitschke, J. R.; Lützen, A. An Octanuclear Metallosupramolecular Cage Designed To Exhibit Spin-Crossover Behavior. *Angew. Chem., Int. Ed.* **2017**, *56*, 4930−4935.
(22) Rizzuto, F. J.; Nitschke, J. R. Stereochemical plasticity modulates cooperative binding in a $Co^{II}_{12}L_6$ cuboctahedron. *Nat. Chem.* **2017**, *9*, 903−908.
(23) (a) Leenders, S. H. A. M.; Gramage-Doria, R. B.; de Bruin, B.; Reek, J. N. H. Transition metal catalysis in confined spaces. *Chem. Soc. Rev.* **2015**, *44*, 433−448. (b) Kuijpers, P. F.; Otte, M.; Dürr, M.; Ivanović-Burmazović, I.; Reek, J. N. H.; de Bruin, B. A Self-Assembled Molecular Cage for Substrate-Selective Epoxidation Reactions in Aqueous Media. *ACS Catal.* **2016**, *6*, 3106−3112. (c) Otte, M.; Kuijpers, P. F.; Troeppner, O.; Ivanović-Burmazović, I.; Reek, J. N. H.; de Bruin, B. Encapsulation of Metalloporphyrins in a Self-Assembled Cubic M_8L_6 Cage: A New Molecular Flask for Cobalt−Porphyrin-Catalysed Radical-Type Reactions. *Chem. - Eur. J.* **2014**, *20*, 4880−4884.
(24) García-Simón, C.; Gramage-Doria, R.; Raoufmoghaddam, S.; Parella, T.; Costas, M.; Ribas, X.; Reek, J. N. H. Enantioselective Hydroformylation by a Rh-Catalyst Entrapped in a Supramolecular Metallocage. *J. Am. Chem. Soc.* **2015**, *137*, 2680−2687.
(25) Colomban, C.; Szalóki, G.; Allain, M.; Gomez, L.; Goeb, S.; Sallé, M.; Costas, M.; Ribas, X. Reversible C_{60} ejection from a metallocage through the redox-dependent binding of a competitive guest. *Chem. - Eur. J.* **2017**, *23*, 3016−3022.
(26) (a) Carreira-Barral, I.; Rodríguez-Blas, T.; Platas-Iglesias, C.; de Blas, A.; Esteban-Gómez, D. Cooperative Anion Recognition in Copper(II) and Zinc(II) Complexes with a Ditopic Tripodal Ligand Containing a Urea Group. *Inorg. Chem.* **2014**, *53*, 2554−2568. (b) Niklas, N.; Heinemann, F. W.; Hampel, F.; Clark, T.; Alsfasser, R. The Activation of Tertiary Carboxamides in Metal Complexes: An Experimental and Theoretical Study on the Methanolysis of AcylatedBispicolylamine Copper(II) Complexes. *Inorg. Chem.* **2004**, *43*, 4663−4673. (c) Mandon, D.; Nopper, A.; Litrol, T.; Goetz, S. Goetz S. Tridentate Coordination of Monosubstituted Derivatives of the Tris(2-pyridylmethyl)amine Ligand to $FeCl_3$: Structures and Spectroscopic Properties of ((2-Bromopyridyl)methyl)bis-(2-pyridylmethyl)amine $Fe^{III}Cl_3$ and (((2-p-Methoxyphenyl)pyridyl)-methyl)Bis(2-pyridylmethyl)] amine $Fe^{III}Cl_3$ and Comparison with the Bis(2-pyridylmethyl)]amine $Fe^{III}Cl_3$ Complex. *Inorg. Chem.* **2001**, *40*, 4803−4806.
(27) Culp, J. T.; Madden, C.; Kauffman, K.; Shi, F.; Matranga, C. Screening Hofmann Compounds as CO_2 Sorbents: Nontraditional Synthetic Route to Over 40 Different Pore-Functionalized and Flexible Pillared Cyanonickelates. *Inorg. Chem.* **2013**, *52*, 4205−4216.
(28) The structure of $L_1Cu^{II}(Br)_2$ shows a monomeric complex where the copper center resides in a square pyramidal geometry. Two pyridines, the tertiary amine, as well as one bromine counterion molecule coordinate in the equatorial plane with the following bond distances: Cu−N1, 2.017 Å; Cu−N2, 2.015 Å; Cu−N3, 2.081 Å; Cu−Br1, 2.407 Å, respectively. The apical position is occupied by the second bromine ion, at the distance Cu−Br2 = 2.639 Å. Complex $L_1Cu^{II}(Cl)_2$ is isostructural with $L_1Cu^{II}(Br)_2$ (Figure S6) and will not be discussed further.
(29) The structure of $L_1Fe^{III}(Cl)_3$ shows a monomeric complex, where the iron center resides in a distorted octahedral geometry. One BPA-pyridine, the tertiary amine, as well as two chloride ions occupy the equatorial coordination plane with the following bond distances: Fe−N1, 2.200 Å; Fe−N3, 2.283 Å; Fe−Cl1, 2.284 Å; Fe−Cl2, 2.295 Å, respectively. The apical positions are occupied by the second-BPA pyridine and one chloride ion, at the following distances: Fe−N2, 2.198 Å; Fe−Cl3, 2.290 Å.
(30) Same host−guest adducts are obtained by reacting the empty cage $1\cdot(BAr^F)_8$ with stoichiometric amounts of the complexes $L_1Zn^{II}(Cl)_2$, $L_1Cu^{II}(Br)_2$, and $L_1Fe^{III}(Cl)_3$.
(31) Niklas, N.; Alsfasser, R. The chemistry of nitrogen coordinated tertiary carboxamides: a spectroscopic study on bis(picolyl)-amidecopper(II) complexes. *Dalton Trans.* **2006**, 3188−3199.
(32) Evans, A. J.; Watkins, S. E.; Craig, D. C.; Colbran, S. B. Copper complexes with ferrocenyl pendants: Evidence for an Fe^{II}-Cu^{II} Fe^{III}-Cu^{I} electron transfer equilibrium leading to a reaction with dioxygen. *J. Chem. Soc., Dalton Trans.* **2002**, 983−994.
(33) Cambré, S.; Wenseleers, W.; Goovaerts, E. Endohedral Copper(II)acetylacetonate/Single-Walled Carbon Nanotube Hybrids, Characterized by Electron Paramagnetic Resonance. *J. Phys. Chem. C* **2009**, *113*, 13505−13514.
(34) Kirin, S. I.; Dubon, P.; Weyhermuller, T.; Bill, E.; Metzler-Nolte, N. Amino Acid and Peptide Bioconjugates of Copper(II) and Zinc(II) Complexes with a Modified *N*,*N*-Bis(2-picolyl)amine Ligand. *Inorg. Chem.* **2005**, *44*, 5405−5415.
(35) Nunes, P.; Nagy, N. V.; Alegria, E. C. B. A.; Pombeiro, A. J. L.; Correia, I. The solvation and redox behavior of mixed ligand copper(II) complexes of acetylacetonate and aromatic diimines in ionic liquids. *Inorg. Chim. Acta* **2014**, *409*, 465−471.
(36) Inokuma, Y.; Arai, T.; Fujita, M. Networked molecular cages as crystalline sponges for fullerenes and other guests. *Nat. Chem.* **2010**, *2*, 780−783.
(37) García-Simón, C.; Garcia-Borràs, M.; Gómez, L.; Parella, T.; Osuna, S.; Juanhuix, J.; Imaz, I.; Maspoch, D.; Costas, M.; Ribas, X. Sponge-like molecular cage for purification of fullerenes. *Nat. Commun.* **2014**, *5*, 5557.
(38) McCarthy, J. R.; Weissleder, R. Model Systems for Fluorescence and Singlet Oxygen Quenching by Metalloporphyrins. *ChemMedChem* **2007**, *2*, 360−365.
(39) Takashima, H.; Kawahara, H.; Kitano, M.; Shibata, S.; Murakami, H.; Tsukahara, K. Metal Ion-Dependent Fluorescent Dynamics of Photoexcited Zinc-Porphyrin and Zinc-Myoglobin Modified with Ethylenediaminetetraacetic Acid. *J. Phys. Chem. B* **2008**, *112*, 15493−15502.
(40) Weng, Y. Q.; Yue, F.; Zhong, Y. R.; Ye, B. A. Copper(II) Ion-Selective On-Off-Type Fluoroionophore Based on Zinc Porphyrin-Dipyridylamino. *Inorg. Chem.* **2007**, *46*, 7749−7755.
(41) Ma, Y.; Li, X.; Li, A.; Yang, P.; Zhang, C.; Tang, B. H_2S-Activable MOF Nanoparticle Photosensitizer for Effective Photodynamic Therapy against Cancer with Controllable Singlet-Oxygen Release. *Angew. Chem., Int. Ed.* **2017**, *56*, 13752−13756.

DOI: 10.1021/acs.inorgchem.7b02852
Inorg. Chem. 2018, 57, 3529−3539

(42) Ding, Y.; Zhu, W. H.; Xie, Y. Development of Ion Chemosensors Based on Porphyrin Analogues. *Chem. Rev.* **2017**, *117*, 2203−2256.
(43) No further evolution of the Soret band wavelength (UV-vis titration) was observed after addition of 2.0 equiv. of the guests $L_1Cu^{II}(Br)_2$ and $L_1Fe^{III}(Cl)_3$, indicating the complete formation of the 1:1 host/guest adduct even in highly diluted conditions (1.12×10^{-6} M), upon addition of 2.0 equiv of the Cu- and Fe-based guests.
(44) Kee, H. L.; Bhaumik, J.; Diers, J. R.; Mroz, P.; Hamblin, M. R.; Bocian, D. F.; Lindsey, J. S.; Holten, D. Photophysical characterization of imidazolium-substituted Pd(II), In(III), and Zn(II) porphyrins as photosensitizers for photodynamic therapy. *J. Photochem. Photobiol., A* **2008**, *200*, 346−355.

DOI: 10.1021/acs.inorgchem.7b02852
Inorg. Chem. 2018, 57, 3529−3539